FOUR DEGREES-OF-FREEDOM MICROMACHINED GYROSCOPES

Cenk Acar[†] **and Andrei M. Shkel**

Microsystems Laboratory, Department of Mechanical and Aerospace Engineering, University of California at Irvine, CA, USA

Abstract

This paper reports a novel design concept for micromachined gyroscopes with inherent disturbance-rejection capabilities. The proposed approach is based on increasing the degrees-of-freedom (DOF) of the oscillatory system by the use of two independently oscillating interconnected proof masses. Utilizing dynamical amplification in the 4-DOF system, inherent disturbance rejection is achieved, providing reduced sensitivity to structural and thermal parameter fluctuations and damping changes over the operating time of the device. In the proposed system, the first mass is forced to oscillate in the drive direction, and the response of the second mass in the orthogonal direction is sensed. The response to the rotation-induced Coriolis force has two resonant peaks and a flat region between peaks. Nominal operation of the device is in the flat region of the response, where the gain is less sensitive to frequency fluctuations. Simulations indicate over 15 times increase in the bandwidth of the system due to the use of the proposed design concept. In addition, the gain in the operation region has low sensitivity to damping changes. Consequently, by utilizing the disturbance-rejection capability of the dynamical system, improved robustness is achieved, which might relax tight fabrication tolerances and packaging requirements, and thus, reduce the production cost of micromachined gyroscopes.

Keywords: MEMS, inertial sensors, micromachined gyroscopes, disturbance rejection

1. Introduction

With the advances in micromachining technologies, low cost inertial micro-sensors on-a-chip are beginning to enter the market. Derived from the conventional Integrated Circuit (IC) fabrication technologies, micromachining processes allow mass-production of microstructures with moving parts on a chip controlled by electronics integrated on the same chip. Optimistic projections predict that in a near future, expensive and bulky conventional inertial sensors will be replaced by their low-cost and micro-sized counterparts without any compromise in performance. Micromachined gyroscopes could potentially provide high accuracy rotation measurements leading to a wide range of applications including navigation and guidance systems, automotive safety systems, and consumer electronics. Gyroscopes are probably the most challenging type of transducers ever attempted to be designed using MEMS technology. Truly low-cost and high-performance devices are not on the market yet. Due to complexity of their dynamics, the current state of the art micromachined gyroscopes require an order of magnitude improvement in performance, stability, and robustness.

All existing micromachined rate gyroscopes operate on the vibratory principle of a single proof mass suspended by flexures anchored to the substrate. The flexures serve as the flexible suspension between the proof mass and the substrate, making the mass free to oscillate in two orthogonal directions - the drive and the sense [1] (Fig. 2a). The proof mass is driven into resonance in the drive direction by an external sinusoidal force. If the gyroscope is subjected to an angular rotation, the Coriolis force is induced in the y-direction. If the drive and sense resonant frequencies are matched, the Coriolis force excites the system into resonance in the sense direction. The resulting oscillation amplitude in the sense direction is proportional to the Coriolis force and, thus, to the angular velocity to be measured.
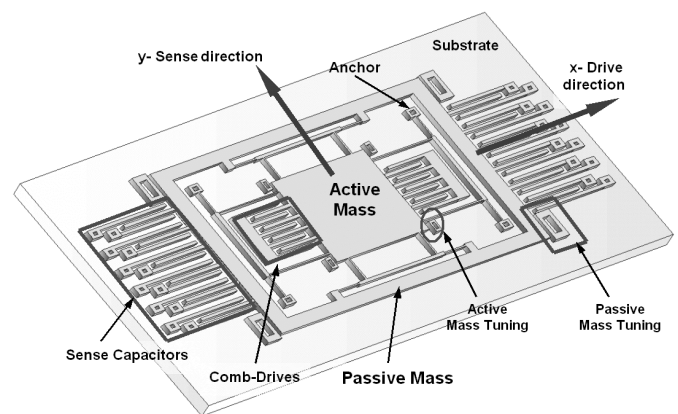

Fig. 1: Conceptual sketch of the micromachined dual-mass z-axis gyroscope.

†cacar@uci.edu

To achieve the maximum possible gain, the conventional gyroscopes are designed to operate at the peak of the response curve. This is typically achieved by matching drive and sense resonant frequencies (Fig. 2b). However, the system is very sensitive to variations in system parameters causing a shift in the resonant frequency. Under high quality factor conditions the gain is high, or the amplitude of the response is large; however the bandwidth is extremely narrow. This results in high sensitivity of the device not only to the Coriolis force, but also to any disturbance in the dynamical system parameters. For example, a 1% fluctuation in frequency matching between drive and sense modes will produce an error of 20% in the output signal gain [4]. In addition, the gain is affected significantly by fluctuations in damping conditions (Fig. 2b).

Fabrication imperfections are inevitable, and affect material properties and geometry of MEMS structures. For surface micromachining, the thickness of the suspension elements is determined by deposition process, and the width is affected by etching process. In addition, Young's Modulus of the structure is affected by deposition conditions. Variations in elastic modulus, beam thickness or residual stresses have drastic effect on dynamic response of gyroscopes, causing resonant frequency shifts or quadrature errors. Generally, very sophisticated control electronics is used to provide operation in the region of the resonance peak [6]. Furthermore, during the operation time of these devices, fluctuations in the ambient temperature alter the gyroscope geometry together with structural properties; and pressure fluctuations affect the damping conditions, resulting in significant errors.

To eliminate the limitations of the existing micromachined gyroscopes, a design approach that does not require the system to operate in resonance is presented in this paper. The proposed architecture suggests the use of two independently vibrating proof masses in the dynamical system (Fig. 1) instead of one, as this is typically done in the conventional devices. The first mass is forced to oscillate in the drive direction, and this forced oscillation is amplified by the second mass. The response of the second mass in the orthogonal sense direction is monitored. The resulting 4-DOF dynamic system has a more favorable frequency response, and can operate in a wider frequency band with insignificant change in the gain. The device is demonstrated to have improved robustness against expected fabrication and packaging fluctuations, especially against damping variations due to ambient pressure. We first present, in Section 2, the design approach and the principle of operation. The dynamics of the device is then analyzed in Section 3, and a MEMS implementation of the design concept is presented in Section 4. The detailed analysis of sensitivity of the device to fabrication variations, temperature fluctuations, and pressure changes is fully developed in Section 5.
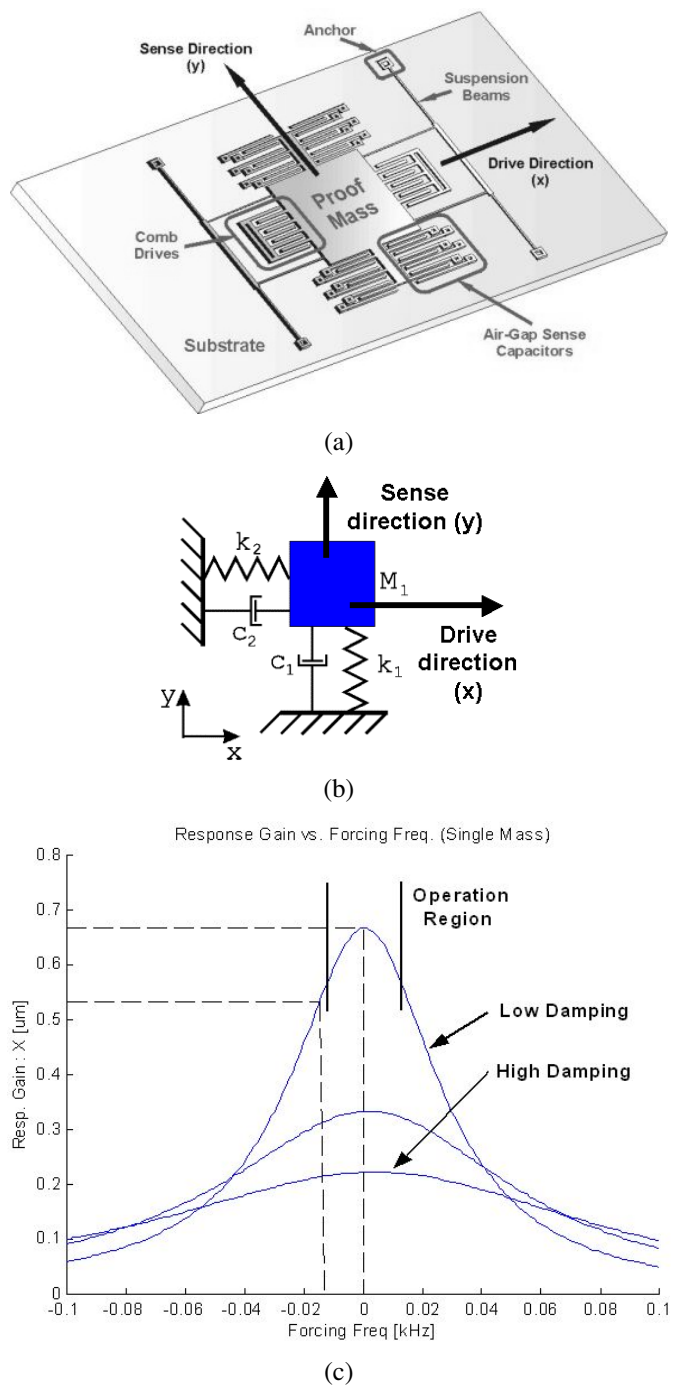

(a)

(b)

(c)

Fig. 2: (a) A conventional rate gyroscope has a single proof mass which is free to oscillate in two principle directions: drive and sense. (b) The lumped model of the overall 2-DOF dynamical system. (c) The response of the system can be viewed as a 1-DOF system excited by the Coriolis force. Note that the gain is very sensitive to matching of drive and sense mode resonant frequencies, as well as damping fluctuations.

2. Design Approach and Principle of Operation

In contrast to the conventional micromachined gyroscopes, the proposed design approach utilizes a 4 degrees-of-freedom (DOF) dynamic system. In order to achieve dynamic amplification of mechanical motion, a system containing two vibrating proof masses (Fig. 4) is used. The increased degrees-of-freedom results in an increased design parameter space, which allows the dynamic response of the gyroscope to be shaped as needed with much less compromise in performance. An implementation of the conceptual design, Fig. 3, is illustrated in Fig. 4 (see details in [9]).
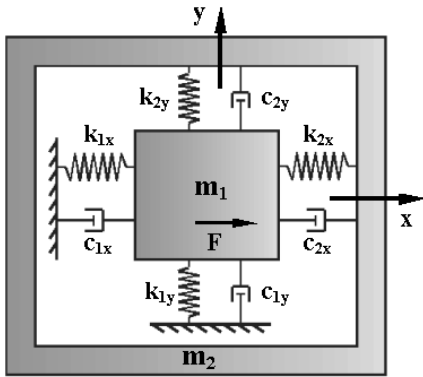

Fig. 3: Lumped mass-spring-damper model of the dual-mass gyroscope. The first mass is driven in the x-direction, and the response of the second mass along the y-axis is sensed.

2.1. Principle of Operation:

The dynamic system of the proposed micromachined gyroscope consists of the following main components: two vibrating proof masses suspended above the substrate, the flexures between the active mass and the ground which are anchored to the substrate, and the flexures between active mass and the passive mass which mechanically couple both masses (Fig. 4).

The gyroscope has two orthogonal principle axes of oscillation: the drive direction (x-axis in Fig. 3) and the sense direction (y-axis in Fig. 3). Both of the proof masses are rendered free to oscillate in the drive and sense directions by the suspension system.

The active mass (m_1 in Fig. 3) is electrostatically forced to oscillate in the drive direction by the comb-drive structures built on each side of the mass (Fig. 4). There is no electrostatic force applied on the passive mass (m_2 in Fig. 3), and the only forces acting on this mass are the elastic coupling forces and the damping forces. The design approach is based on dynamically amplifying the oscillation of the active mass by the passive mass, as will be explained in Section 4.3. The response of the passive mass in the sense direction to the rotation-induced Coriolis force is monitored by the air-gap sense capacitors built around the passive mass, Fig. 4, providing the angular rate information.

With appropriate selection of dynamical system parameters including the masses and the spring rates, one can obtain the frequency response in the sense direction of the gyroscope illustrated in Fig. 5. There exists three regions of interest on this response curve: two resonant peaks, regions 1 and 3; and a flat region between the peaks, region 2. According to the proposed design approach, the nominal operation of the gyroscope is in the flat region, where the signal gain is relatively high, and the sensitivity of the gain to driving frequency variations is low. Because of the widened bandwidth, a 1% variation in natural frequencies of the system results in only 0.8% error in the output signal, whereas the same fluctuation will produce an error of 20% in the conventional micromachined gyroscopes [4].
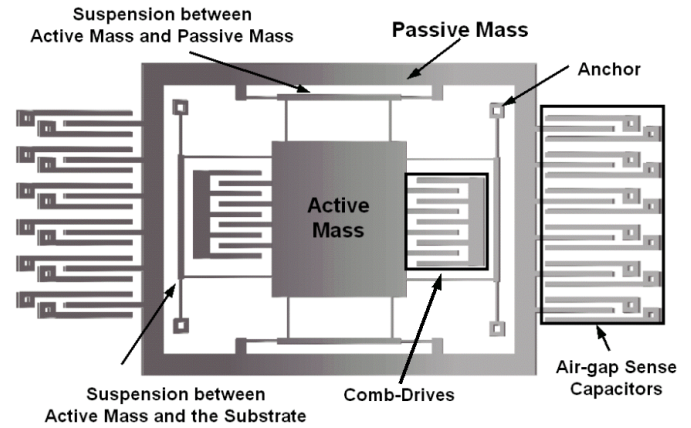

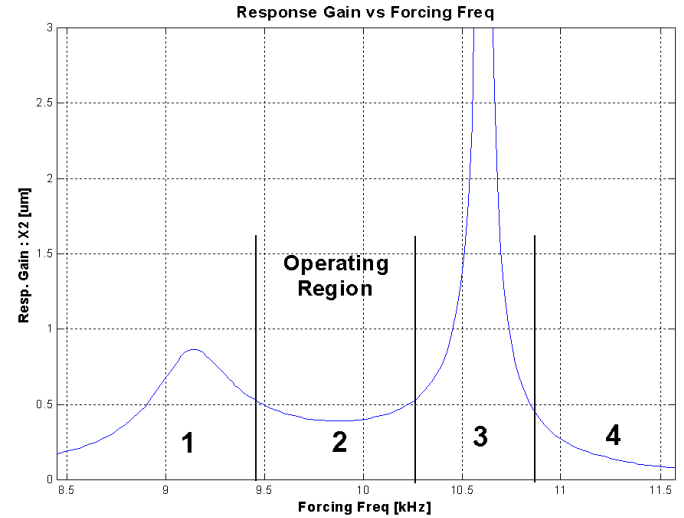Fig. 4: Schematic illustration of a MEMS implementation of the dual-mass z-axis gyroscope.

Fig. 5: Response of the dual-mass gyroscope in the flat operation region is insensitive to resonant frequency fluctuations and has over 15 times wider bandwidth than in conventional gyroscopes
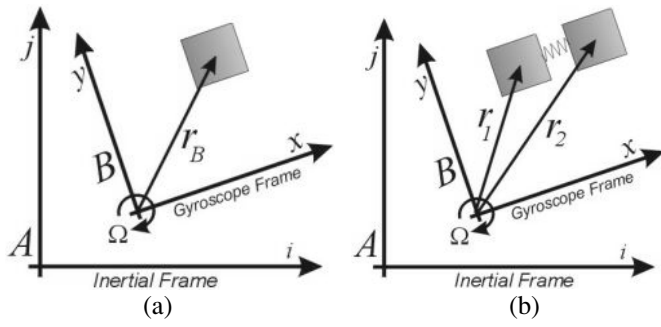
Fig. 6: (a) Representation of the position vector of a body relative to the rotating frame. (b) Representation of the position vectors of the proof masses of the gyroscope relative to the rotating "gyroscope frame" B.

3. Dynamics of the Gyroscope

The dynamics of the gyroscope should be considered in the non-inertial frame. Referring to Fig. 6, the expression of absolute acceleration (in the inertial frame) of a rigid body with the position vector $\vec{r}$ attached to a rotating reference frame *B* is

$$\vec{a_A} = \vec{a_B} + \vec{\Omega} \times \vec{r_B} + \vec{\Omega} \times (\vec{\Omega} \times \vec{r_B}) + 2\vec{\Omega} \times \vec{v_B}$$

where the subscript *A* denotes "relative to inertial frame *A*", *B* denotes "relative to rotating gyroscope frame *B*", $\vec{v_B}$ and $\vec{a_B}$ are the velocity and acceleration vectors with respect to the reference frame respectively, $\vec{\Omega}$ is the angular velocity of the gyroscope frame, and "×" operation refers to cross-product

of two vectors. The reference rotating gyroscope frame is assumed to be non-accelerating. The last term $2\vec{\Omega} \times v_B$ in the equation, the Coriolis term, is of special interest since the operation of the gyroscope depends on excitation of system in the sense direction by the Coriolis force due to this term. Thus, for a mass driven into oscillation in the x-direction, and subject to an angular rate of Ω_z about the z-axis, the Coriolis acceleration induced in the y-direction reduces to

$$a_y = 2\Omega_z \dot{x}(t)$$

Similarly, when the active and passive masses are observed in the non-inertial rotating frame, the "gyroscope frame", additional inertial forces appear acting on both masses. The equations of motion for the two-mass system can be written as:

$$m_1\vec{a_1} = \overrightarrow{F_{2-1}} + \overrightarrow{F_{s-1}} - 2m_1\vec{\Omega} \times \vec{v_1} - m_1\vec{\Omega} \times (\vec{\Omega} \times \vec{r_1}) - m_1\dot{\vec{\Omega}} \times \vec{r_1}$$

$$m_2\vec{a_2} = \overrightarrow{F_{1-2}} + \overrightarrow{F_{s-2}} - 2m_2\vec{\Omega} \times \vec{v_2} - m_2\vec{\Omega} \times (\vec{\Omega} \times \vec{r_2}) - m_2\dot{\vec{\Omega}} \times \vec{r_2}$$

where $\vec{r_1}$ and $\vec{r_2}$ are the position vectors, $\vec{v_1}$ and $\vec{v_2}$ are the velocity vectors of the masses defined in the gyroscope frame, $\overrightarrow{F_{2-1}}$ and $\overrightarrow{F_{1-2}}$ are the opposing coupling forces between the masses that each mass applies on other depending on relative position $\vec{r_2} - \vec{r_1}$, including spring and damping forces. $\overrightarrow{F_{s-1}}$ consists of spring and damping forces between the active mass and the substrate, and $\overrightarrow{F_{s-2}}$ includes the passive mass - substrate damping force. Since both masses are subject to an angular rate of Ω_z about the axis normal to the plane of operation (z-axis), the equations of motion along the x-axis and y-axis become:

$$m_1\ddot{x}_1 + c_{1x}\dot{x}_1 + k_{1x}x_1 = (k_{2x}(x_2 - x_1) + c_{2x}(\dot{x}_2 - \dot{x}_1) + m_1\Omega^2 x_1 - 2m_1\Omega\dot{y}_1 + m_1\dot{\Omega}y_1 + F_d(t))$$

$$m_2\ddot{x}_2 + c_{2x}(\dot{x}_2 - \dot{x}_1) + k_{2x}(x_2 - x_1) = (m_2\Omega^2 x_2 - 2m_2\Omega\dot{y}_2 + m_2\dot{\Omega}y_2)$$

$$m_1\ddot{y}_1 + c_{1y}\dot{y}_1 + k_{1y}y_1 = (k_{2y}(y_2 - y_1) + c_{2y}(\dot{y}_2 - \dot{y}_1) + m_1\Omega^2 y_1 - 2m_1\Omega\dot{x}_1 + m_1\dot{\Omega}x_1)$$

$$m_2\ddot{y}_2 + c_{2y}(\dot{y}_2 - \dot{y}_1) + k_{2y}(y_2 - y_1) = (m_2\Omega^2 y_2 - 2m_2\Omega\dot{x}_2 + m_2\dot{\Omega}x_2)$$

(1)

where $F_d(t)$ is the driving electrostatic force applied to the active mass, and Ω is the angular velocity applied to the gyroscope about the z-axis.

The overall dynamic model can be reduced having the active mass driven into forced oscillation in drive direction by $F_d(t)$ with a constant amplitude x_0 and a frequency ω_d. Assuming

the oscillation of the first mass in the drive direction is set by the control system to be

$$x_1 = x_0\cos(\omega_d t),$$

the system (11) reduces to 3 degrees of freedom. The equations of motion of the reduced system become [4]:

$$\ddot{y}_1 + 2\omega_n\xi\dot{y}_1 + 2\mu\omega_n\xi(\dot{y}_1 - \dot{y}_2) + (\omega_n - \Omega)y_1 + \omega_n^2\sigma_1(y_1 - y_2) = -2\Omega\omega_d x_0\sin\omega_d t + \dot{\Omega}x_0\cos\omega_d t$$

$$\beta(\ddot{y}_2 - \Omega^2 y_2) + 2\mu\omega_n\xi(\dot{y}_2 - \dot{y}_1) - 2\beta\Omega\dot{x}_2 - \beta\dot{\omega}_z x_2 + \omega_n^2\sigma_1(y_2 - y_1) = 0$$

(2)

$$\beta(\ddot{x}_2 - \Omega^2 x_2) + 2\beta\Omega\dot{y}_2 + \beta\dot{\Omega}y_2 + \omega_n^2\sigma_2 x_2 = \omega_n^2\sigma_2 x_0\cos\omega_d t$$

where $\beta = m_2/m_1$, $\sigma_1 = k_{2y}/k_{1y}$, $\sigma_2 = k_{2x}/k_{1x}$, $\mu = c_2/c_1$, $\xi = c_1/2m_1\omega_n$, and ω_n is the natural frequency in the sense direction. Proper selection of system parameters including the

masses m_1 and m_2, the spring constants k_{1x}, k_{1y}, k_{2x}, and k_{2y} will result in the frequency response illustrated in Fig. 5.

4. Implementation of the Design Concept

This section describes the principle elements of a MEMS implementation of the conceptual design presented in Section 2. First the stiffness and the damping components of the dynamic system are analyzed, and then the issue of achieving dynamic amplification in the drive mode is addressed.
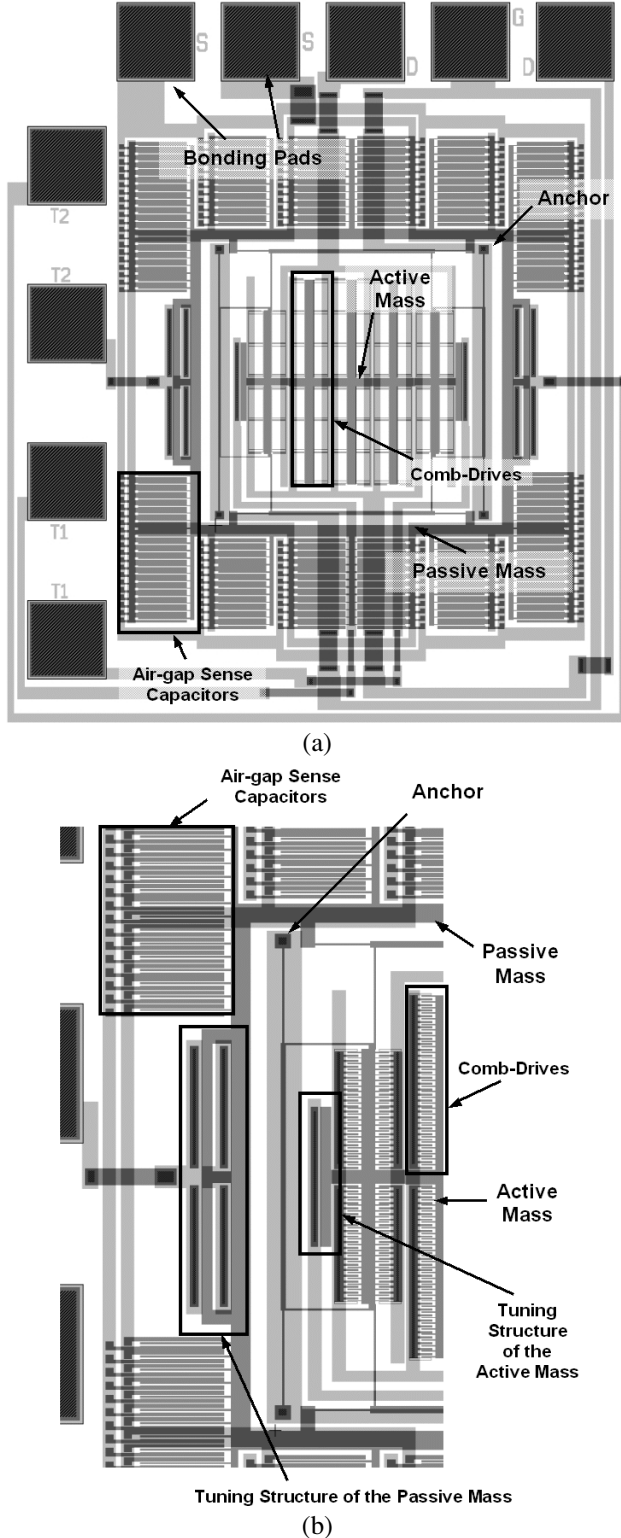

(a)

(b)

Fig. 7: The layout of the dual-mass z-axis gyroscope.

4.1. Suspension Design

The complete suspension system of the device consists of two sets of four flexible beams per each mass. For each proof mass, one set of fixed-guided beams provides the desired spring rate in the drive direction, while the other set provides the desired spring rate in the sense direction [9]. For a single fixed-guided beam, the translational stiffness in the orthogonal direction to the axis of the beam is given by [10]

$$k_y = \frac{1}{2}\frac{3EI}{\frac{L^3}{2}} = \frac{Etw^3}{L^3}$$

where E is the Young's Modulus, and I is the second moment of inertia. The beam length, thickness, and width are L, t, and w, respectively.

Spring rates for a mass in drive or sense direction are determined by four fixed-guided beams if the axial strains in the other beams are neglected. This assumption is reasonable in this analysis, since the axial stiffness of a beam, $k_{axial} = Etw/L$, is generally four orders of magnitude (L^2/w^2 times) larger than the fixed-guided stiffness, which means the beams under axial load can be assumed infinitely stiff. Thus, each stiffness value in the dynamic system can be calculated as

$$k_{1x} = \frac{4Etw^3}{L_{1x}^3} \quad k_{1y} = \frac{4Etw^3}{L_{1y}^3} \quad k_{2x} = \frac{4Etw^3}{L_{2x}^3} \quad k_{2y} = \frac{4Etw^3}{L_{2y}^3}$$

where w and t are the width and thickness of the beam elements in the suspension, respectively. The individual beam lengths are shown in Fig. 8. Finite element analysis of the gyroscope is performed using the software package ANSYS[TM] to validate the assumptions in the theoretical analysis. The resonant frequencies obtained from modal analysis results matched the theoretical calculations within 0.1% error. Furthermore, the unwanted resonant modes were observed to be over 4 kHz higher than the nominal operational frequency.
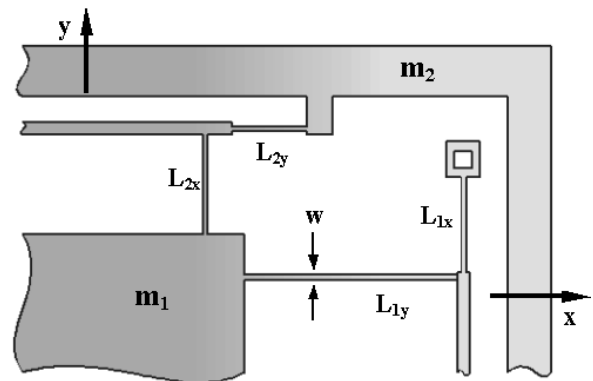

Fig. 8: Suspension system configuration provides two degrees of freedom (in drive and sense directions) for the active proof mass and the passive proof mass.
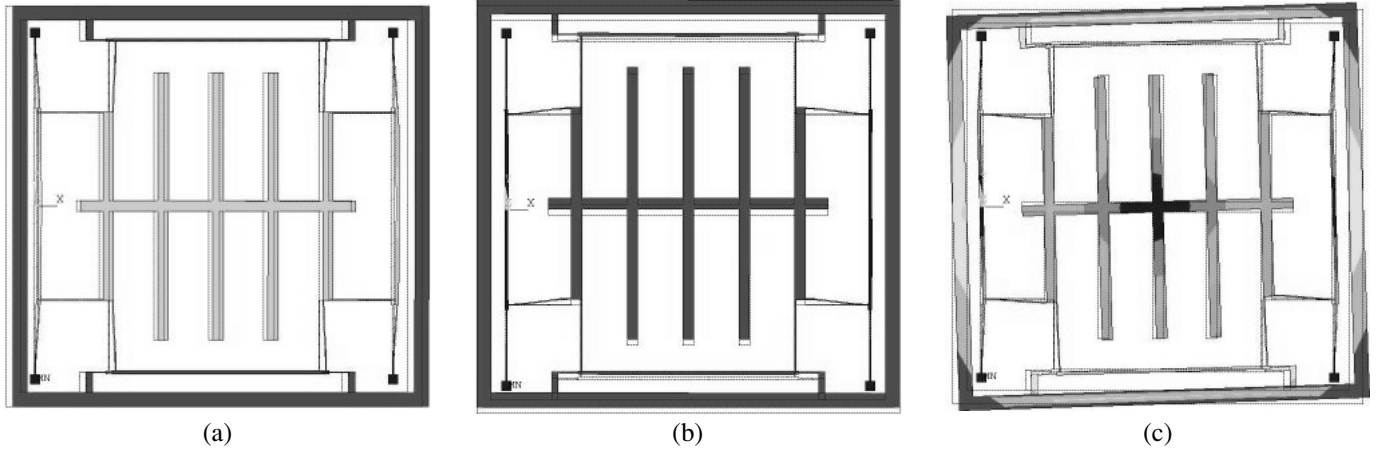
(a)   (b)   (c)

Fig. 9: The first three resonant modes of the gyroscope. The simulation is performed using the finite element analysis package ANSYS[TM].
FEA results were observed to agree with the theoretical analysis within 0.1% error.

4.2. Damping Estimation

The four damping coefficients (c_{1x}, c_{1y}, c_{2x}, and c_{2y}) in the dynamical system shown in Fig. 3 are due to the viscous effects of the air between the masses and the substrate, and in between the comb-drive and sense capacitor fingers. For the active mass, the total damping in the drive mode can be expressed as the sum of damping due to Couette flow between the mass and the substrate, and the damping due to Couette flow between the integrated comb fingers [2]:

$$c_{1x} = \mu_p p \frac{A_1}{z_0} + \mu_p p \frac{2N_{comb}l_{comb}t}{y_{comb}}$$

where A_1 is the area of the active mass, z_0 is the elevation of the proof mass from the substrate, t is the thickness of the structure, N_{comb} is the number of comb-drive fingers, y_{comb} is the distance between the fingers, l_{comb} is the length of the fingers, p is the ambient pressure within the cavity of the packaged device, and μ_p= 3.7 10^{-4} kg/(m^2.s.torr) is the viscosity constant for air.

In the sense mode, the total damping is the sum of damping due to Couette flow between the proof mass and the substrate, and the squeeze film damping between the integrated comb fingers [2]:

$$c_{1y} = \mu_p p \frac{A_1}{z_0} + \mu_p p \frac{7N_{comb}l_{comb}t^3}{y_{comb}}$$

However, for the passive mass, the total damping in the drive mode results from Couette flow between the mass and the substrate, as well as Couette flow between the air-gap capacitor fingers [2]:

$$c_{2x} = \mu_p p \frac{A_2}{z_0} + \mu_p p \frac{2N_{capacitor}l_{finger}t}{y_{capacitor}}$$

where A_2 is the area of the passive mass, $N_{capacitor}$ is the number of air-gap capacitors, $y_{capacitor}$ is the distance between the capacitor fingers, and $l_{capacitor}$ is the length of the fingers.

Damping of the passive mass in the sense mode can be estimated as the combination of Couette flow between the proof mass and the substrate, and the Squeeze Film damping between the air-gap capacitor fingers [2]:

$$c_{2y} = \mu_p p \frac{A_2}{z_0} + \mu_p p \frac{7N_{capacitor}l_{finger}t^3}{y_{capacitor}^3}$$

These pressure dependent effective damping values will be used in the parametric sensitivity analysis simulations of the dynamic system.
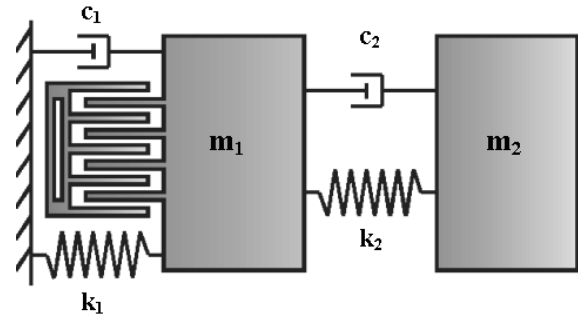

Fig. 10: Lumped model of the drive mode of dual-mass gyroscope. The passive mass (m_2) acts as a vibration absorber, to amplify the motion of the active mass (m_1).

4.3. Dynamic Amplification in Drive Mode

To achieve the maximum possible response of the gyroscope, amplitude of the drive-direction oscillation of the passive mass should be maximized. In the drive mode, the dynamic system is simply a 2-DOF system. A sinusoidal force is applied on the active mass by the comb-drive structure. Assuming a lumped parameter model, the equations of motion in the drive mode become:

$$m_1\ddot{x}_1 + c_1\dot{x}_1 + (k_1 + k_2)x_1 = F + k_2 x_2$$

$$m_2 x_2 + c_2 x_x + k_2 x_2 = k_2 x_1$$

When a sinusoidal force $F = F_0\sin(\omega t)$ is applied on the active mass by the interdigitated comb-drives, the steady-state response of the 2-DOF system will be

$$X_1 = \frac{F_0}{k_1} \frac{1 - \left(\dfrac{\omega}{\omega_2}\right)^2 + j\omega\dfrac{c_2}{k_2}}{\left[1 + \dfrac{k_2}{k_1} - \left(\dfrac{\omega}{\omega_1}\right)^2 + j\omega\dfrac{c_1}{k_1}\right]\left[1 - \left(\dfrac{\omega}{\omega_2}\right)^2 + jw\dfrac{c_2}{k_2}\right] - \dfrac{k_2}{k_1}}$$

$$X_2 = \frac{F_0}{k_1} \frac{1}{\left[1 + \dfrac{k_2}{k_1} - \left(\dfrac{\omega}{\omega_1}\right)^2 + j\omega\dfrac{c_1}{k_1}\right]\left[1 - \left(\dfrac{\omega}{\omega_2}\right)^2 + jw\dfrac{c_2}{k_2}\right] - \dfrac{k_2}{k_1}}$$

where $\omega_1 = \sqrt{k_1/m_1}$ and $\omega_2 = \sqrt{k_2/m_2}$ are the resonant frequencies of the isolated active and passive mass-spring systems, respectively. When the driving frequency ω_{drive} is matched with the resonant frequency of the isolated passive mass-spring system, i.e. $\omega_{drive} = \sqrt{k_{2x}/m_{2x}}$, the passive mass moves to exactly cancel out the input force F applied on the active mass, and maximum dynamic amplification is achieved [7].
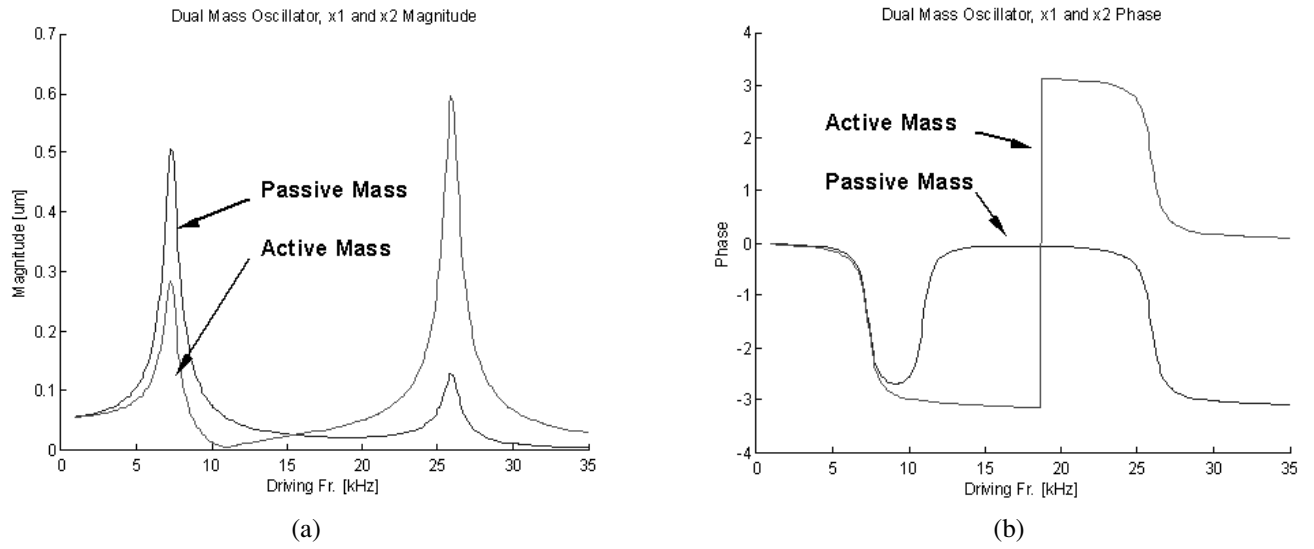

(a)

(b)

Fig. 11: (a) The magnitude plots of each proof mass. At the antiresonant frequency, which is the resonant frequency of the isolated passive mass-spring system, oscillation amplitude of the active mass approaches to zero. (b) The phase plots of each proof mass.
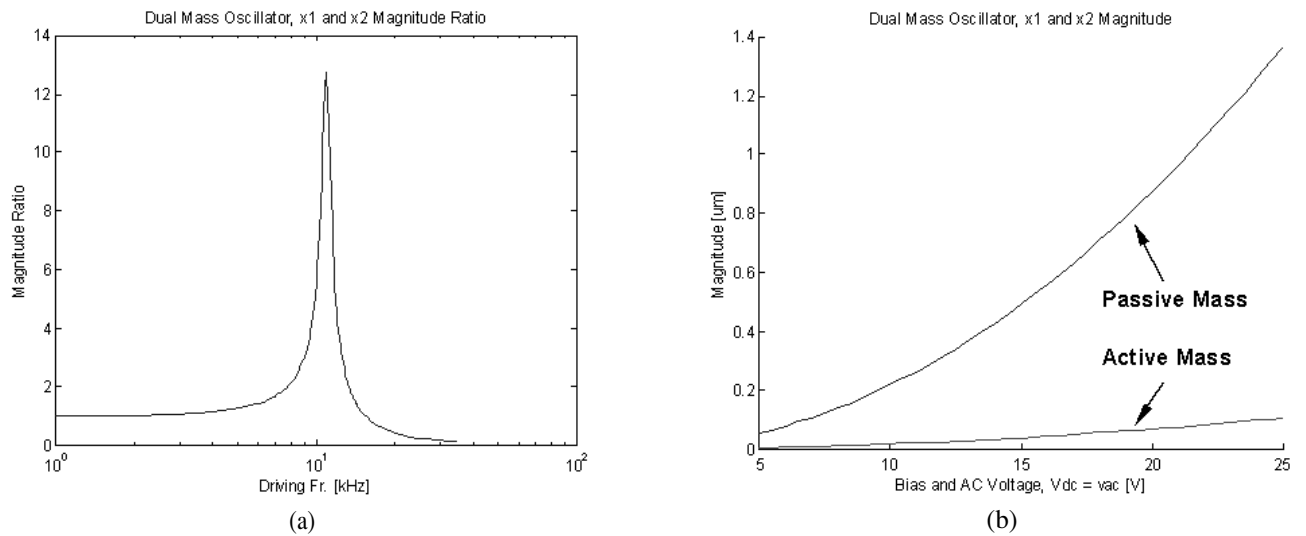

(a)

(b)

Fig. 12: (a) The dynamic amplification ratio reaches its maximum at the antiresonant frequency, i.e., $\omega_{drive} = \sqrt{k_{2x}/m_{2x}}$. (b) With a balanced interdigitated comb-drive scheme, a 1 um amplitude is achieved by the passive mass with a bias voltage of about 20V.

The values of oscillation amplitude in the drive-direction can be calculated knowing the magnitude of sinusoidal force $F = F_0 \sin(\omega t)$ applied on the active mass by the comb-drive structure. Applying $V_1 = V_{DC} + v_{AC}$ to one set of comb drives (e.g. the set on the right side in Fig. 4, and $V_2 = V_{DC} + v_{AC}$ to the opposing set (the set on the left side), a balanced interdigitated comb-drive scheme can be imposed. With this driving scheme, the resulting net electrostatic force is linear to v_{AC}, which will lead to simplification of the dynamic model:

$$ F = 4 \frac{\varepsilon_0 z_0 N}{y_0} V_{DC} v_{AC} $$

where $v_{AC} = |v_{AC}| \sin \omega t$ is the sinusoidal voltage, V_{DC} is the constant bias voltage, z_0 is the finger thickness, and y_0 is the finger separation. Thus, for the gyroscope, the magnitude of the applied drive force is simply

$$ F_0 = 4 \frac{\varepsilon_0 z_0 N}{y_0} V_{DC} |v_{AC}|. $$

With this balanced interdigitated comb-drive scheme, a 1 μm oscillation amplitude is achieved by the passive mass in atmospheric pressure when a bias voltage of about 20V and a 5V alternating voltage is applied.

5. Parametric Sensitivity Analysis

5.1. Fabrication Variations

Fabrication variations can affect the parameters of gyroscopes directly. For micromachining processes, the dimensions of the suspension beam elements are uncertain for different reasons. The length of the beams are determined solely by lithography,

and are extremely accurate. However, the thickness is determined by deposition process, and the width set by lithography is affected by etching process. Thus, these two parameters are less accurate, and can vary by 1% from wafer to wafer.

In conventional gyroscopes, fabrication variations result in resonant frequency shifts, requiring compensation by sophisticated control electronics. Yet, for the proposed system, a 0.05 μm deviation from 2 μm nominal beam width or a 0.1 μm deviation from 2 μm nominal structure thickness results in less than 1% error in the gain (Fig. 15a and Fig. 15b, respectively). Moreover, a variation in deposition conditions that affect the Young's Modulus of the gyroscopes structure by 10 GPa causes less than 0.5 % error (Fig. 15c). The same parameter variations in a conventional micromachined gyroscope without compensation by control electronics result in over 10% error.

5.2. Pressure Fluctuations

Pressure fluctuations can have significant effects on resonance dependent conventional gyroscopes (Fig. 2). In contrast, since the proposed device utilizes dynamic amplification of mechanical motion, and does not operate in resonance, the response is insensitive to damping changes in the operation region. For a possible vacuum leakage from 100 militorrs to 500 militorrs, e.g. due to package sealing degradation over the operation time of the device, the response gain reduces by less than 2% (Fig. 15d), where the same pressure variation can result in over 20% gain reduction in a conventional gyroscope design.
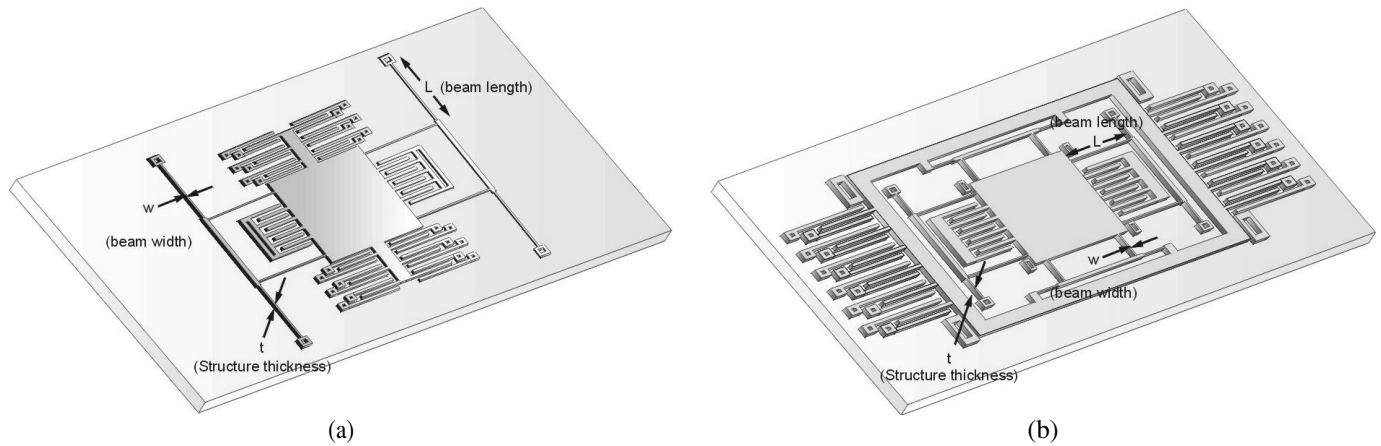

(a) (b)

Fig. 13: Fabrication variations can affect the geometry of the device by varying thickness of the structure or the width of the suspension beam elements. The proposed design illustrated in (b) is demonstrated to be more robust against these variations than the conventional approach illustrated in (a).
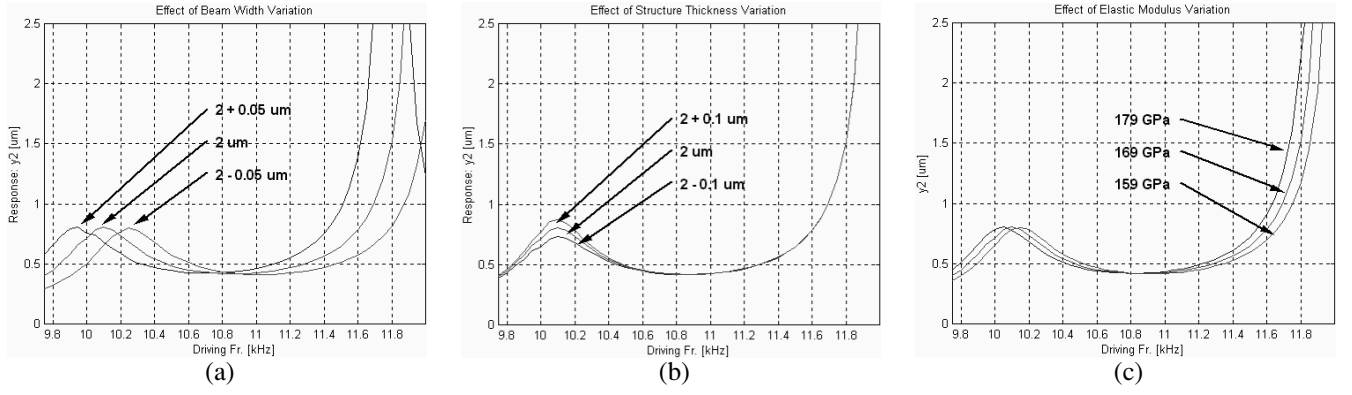
Fig. 14: Change in the response due to: (a)0.05 μm variation in the width of suspension beams, (b)0.1 μm variation in structure thickness, (c) 10 GPa variation in Young's Modulus.
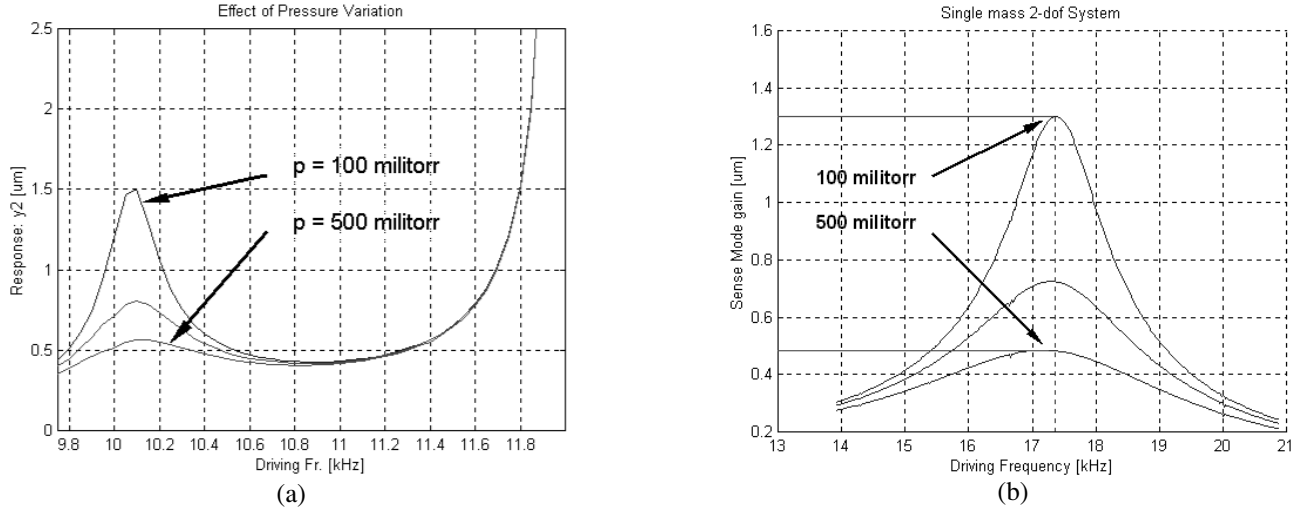

Fig. 15: (a) Ambient pressure change form 100 militorrs to 500 militorrs results in 2% gain reduction for the proposed gyroscope design, (b) The same pressure change causes over 40 times more gain reduction for a conventional gyroscope design with similar geometry.

5.3. Thermal Fluctuations

Variations in the temperature of the structure can perturb the dynamical system parameters by three means: due to the inherent temperature dependence of Young's Modulus, due to changes in suspension geometry because of thermal expansion, and due to the thermally induced localized stress effects. Young's modulus of the structure at a given temperature can be calculated by [8]:

$$E_{0^0C + \Delta T} = E_{0^0C} TC_E \Delta T + E_{0^0C}$$

where E_{0^0C} is the Young's modulus for fine-grained polysilicon at 0 ^{0}C (assumed 169 GPa), TC_E is the temperature coefficient of Young's modulus for polysilicon (assumed [8] -75 ppm/^{0}C), and ΔT is the temperature

change. To reflect the effects of temperature dependent elastic modulus and thermal expansion on the resonant frequency of linear microresonators with folded-beam suspensions, the temperature coefficient of the resonance frequency can be determined as [8]:

$$TC_f = \frac{1}{2}(TC_E - TC_h)$$

where TC_E is the temperature coefficient of the Young's modulus, and TC_h is the temperature coefficient of thermal expansion, which is assumed 2.5 ppm/^{0}C; leading to a perturbed resonant frequency of

$$\omega_{n_0{}^0C + \Delta T} = \omega_{n_0{}^0C} TC_f \Delta T + \omega_{n_0{}^0C}$$
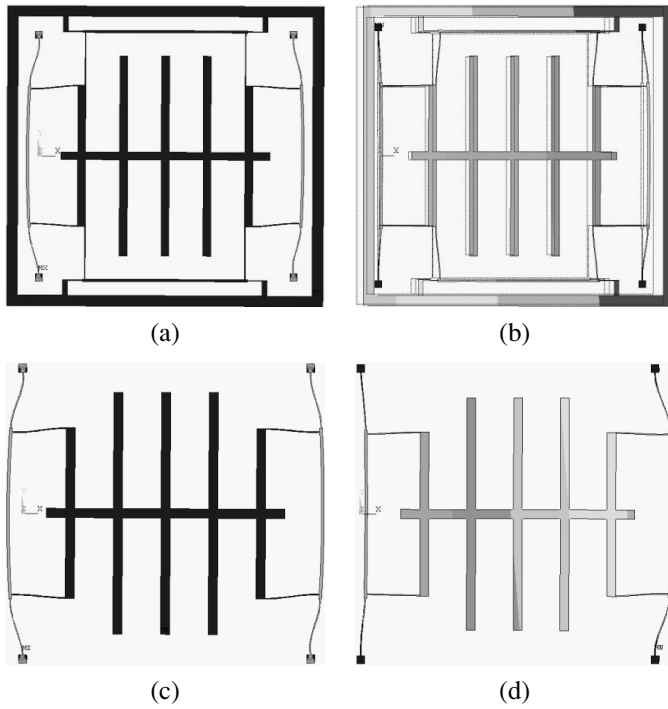
79

(a) (b)

(c) (d)

Fig. 16: (a) Finite element simulation of the device with a uniform temperature loading of 100 ^{0}C. Thermally induced localized stresses were observed only in the drive-direction beam elements of active mass, effecting only k_{1x}. (b) Static finite element analysis of the thermally loaded system with the modified Young's modulus. (c) Finite element analysis of a conventional gyroscope with similar geometry, under the same thermal loading. (d) Static analysis of the conventional design indicate the localized stresses leading to frequency mismatch between the drive and the sense resonant frequencies.

However, for the proposed suspension system, more accurate results can be found conducting finite element analysis of the system. To be able to capture parameter changes due to the temperature dependence of Young's Modulus, due to thermal expansion generated alteration in suspension geometry, and due to thermally induced stresses; a finite element model of the device was created using the finite element analysis software package ANSYS^{TM}. First, a uniform temperature loading of 100 ^{0}C was applied to each surface, and the thermally induced localized stresses were observed. The results of the thermal finite element simulation indicated that a stress of 82 MPa was induced only in the drive-direction beam elements of active mass, effecting only k_{1x}. The other beam elements of the suspension system were observed stress-free (Fig. 17a). Then, static structural analysis of the thermally loaded system with the modified Young's modulus was performed to calculate each of the four spring rates (k_{1x}, k_{1y}, k_{2x}, and k_{2y}) in the dynamical system shown in Fig. 3. The same procedure was also carried out for a uniform temperature loading of -100 ^{0}C. The simulation of the dynamical system with the perturbed parameters due to thermal loading indicated a deviation of less than 0.9% in the

gain. Finite element analysis of a conventional gyroscope with similar geometry demonstrated about 7% gain error for the same thermal loading.
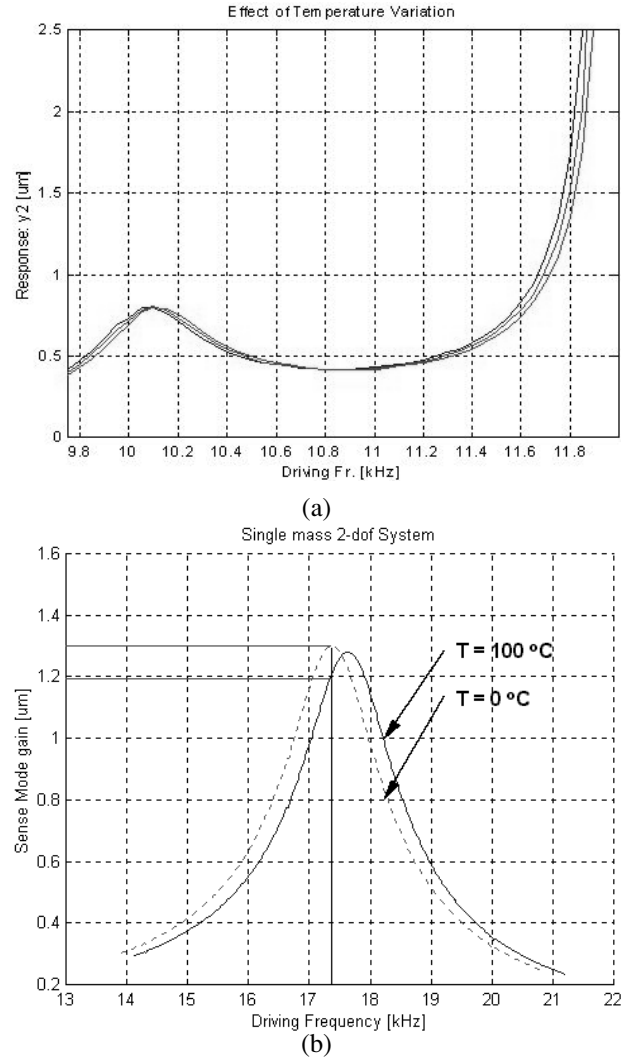

(a)

(b)

Fig. 17: (a) Simulation of the proposed design's dynamical system with the perturbed parameters due to thermal loading was performed, indicating less than 0.9% gain deviation. (b) Simulation of the conventional design with the perturbed parameters indicates 7% gain error for the same thermal loading.

5.4. Residual Stresses

Accumulation of residual stresses in the structure directly affect the properties of the dynamical system. In the presence of residual stresses, the beam stiffness values, and thus the overall system spring rates change. Axial residual stresses in x direction effect only the y-direction spring rates (k_{1y} and k_{2y}) of the suspension, while axial residual stresses in y direction effect only the x-direction spring rates (k_{1x} and k_{2x}).

Thus, for the suspension system with an x-direction axial residual stress of ε_x and a y-direction axial residual stress of ε_y, the spring rate values become [3]

$$k_{1x} = \frac{Etw\kappa_y^2}{12L_{1x}} \left[1 - \frac{2w}{\beta_{1x}L_{1x}} \frac{\cosh\left(\frac{\kappa_y L_{1x}}{w}\right)-1}{\sinh\left(\frac{\kappa_y L_{1x}}{w}\right)} \right] - 1,$$

$$k_{1y} = \frac{Etw\kappa_x^2}{12L_{1y}} \left[1 - \frac{2w}{\beta_{1y}L_{1y}} \frac{\cosh\left(\frac{\kappa_x L_{1y}}{w}\right)-1}{\sinh\left(\frac{\kappa_x L_{1y}}{w}\right)} \right] - 1,$$

$$k_{2x} = \frac{Etw\kappa_y^2}{12L_{2x}} \left[1 - \frac{2w}{\beta_{2x}L_{2x}} \frac{\cosh\left(\frac{\kappa_y L_{2x}}{w}\right)-1}{\sinh\left(\frac{\kappa_y L_{2x}}{w}\right)} \right] - 1,$$

$$k_{2y} = \frac{Etw\kappa_x^2}{12L_{2y}} \left[1 - \frac{2w}{\beta_{2y}L_{2y}} \frac{\cosh\left(\frac{\kappa_x L_{2y}}{w}\right)-1}{\sinh\left(\frac{\kappa_x L_{2y}}{w}\right)} \right] - 1,$$

where $\kappa_x = \sqrt{12\varepsilon_x}$, $\kappa_y = \sqrt{12\varepsilon_y}$ are the dimensionless strain factors for beam bending, and $\beta_{1x} = L_{1x}w/\kappa_y$, $\beta_{1y} = L_{1y}t/\kappa_x$, $\beta_{2x} = L_{2x}w/\kappa_y$, and $\beta_{2y} = L_{2y}t/\kappa_x$.

However, an axial residual stress ε_x in the x direction effects the sense-direction spring rates (k_{1y} and k_{2y}) of the same order, and an axial residual stress ε_y in the y direction effects the drive-direction spring rates (k_{1x} and k_{2x}) of the same order as well. In result, the overall system response is less sensitive to residual stresses (Fig. 18). To compare the sensitivity of the proposed device to the conventional approach, the designed system and a single mass gyroscope with the same geometry of the isolated active mass-spring system were simulated with a 10 MPa compression residual stress. The single-mass system experienced approximately 2.5% gain reduction, while the proposed device experienced less than 0.2% deviation in the gain.

6. Conclusion

A new micromachined gyroscope design with inherent disturbance-rejection is presented, the dynamical system and the design implementation are analyzed, and effects of realistic parameter variations on the system response are investigated. The implementation of the idea is based on the use of two independently oscillating proof masses. By utilizing dynamical amplification, the necessity of operation in the resonance mode is eliminated, and over 15 times increase in the bandwidth of the system is achieved compared to the conventional micromachined gyroscopes. The proposed device is also demonstrated to have improved robustness against expected fabrication and packaging fluctuations, especially against damping variations due to ambient pressure. Sensitivity analysis revealed that, for the same thermal loading, the device produces 87% less error than conventional gyroscopes. Moreover, the proposed design was shown to be approximately 12 times less sensitive to residual stresses, and 20 times less sensitive to fabrication variations than conventional gyroscopes. Consequently, with the presented design approach, tight fabrication tolerances and packaging requirements can be relaxed resulting in a lower production cost of MEMS gyroscopes without compensation in performance.
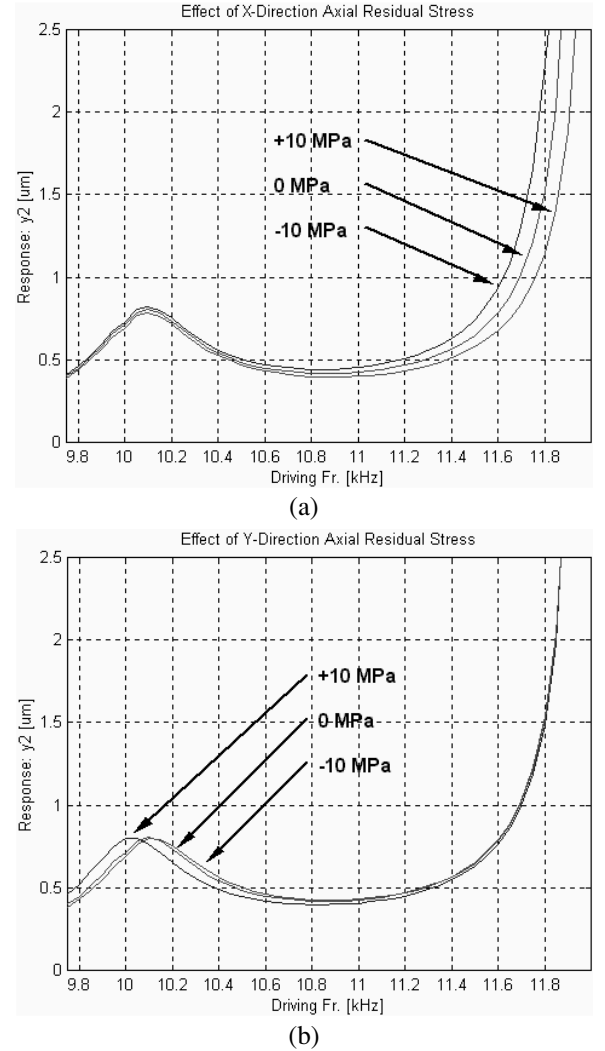

(a)

(b)

Fig. 18: Effect of residual stresses (a) in x-direction, (b) in y-direction.

References

[1]   N. Yazdi, F. Ayazi, and K. Najafi, Micromachined Inertial Sensors., *Proc. of IEEE*, Vol. 86, No. 8, August 1998.

[2]   W.A. Clark, Micromachined Vibratory Rate Gyroscope., *Ph.D. Thesis, BSAC, U.C. Berkeley*, 1994.

[3]   W.A. Clark, R.T. Howe, and R. Horowitz, Surface Micromachined Z-Axis Vibratory Rate Gyroscope, *Proceedings of Solid-State Sensor and Actuator Workshop*, June 1994.

[4]   E. Netzer, and I. Porat, A Novel Vibratory Device for Angular Rate Measurement, *Journal of Dynamic Systems, Measurement and Control*, Dec. 1995.

[5]   A. Shkel, R.T. Howe, and R. Horowitz, Micromachined Gyroscopes: Challenges, Design Solutions, and Opportunities., *Int. Workshop on Micro-Robots, Micro-Machines and Systems, Moscow, Russia*,1999.

[6]   A. Shkel, R. Horowitz, A. Seshia, S. Park and R.T. Howe, Dynamics and Control of Micromachined Gyroscopes, *American Control Conference, CA* ,1999.

[7]   C.W. Dyck, J. Allen, R. Hueber, Parallel Plate Electrostatic Dual Mass Oscillator, *Proceedings of SPIE SOE, CA*, 1999.

[8]   L. Lin, R.T. Howe, and A.P. Pisano, Microelectromechanical Filters for Signal Processing, *Journal of Microelectromechanical Systems, Vol. 7*, Sept.1998.

[9]   C. Acar and A. Shkel, Wide Bandwidth Micromachined Gyroscope to Measure Rotation, *Patent pending, UCI Office of Technology Alliances*, Case No:2001-140-1.

[10] W.C. Young, Roark's Formulas for Stress & Strain, *McGraw-Hill, Inc.*, 93-156, 1989.

[11] A. Lawrence, Modern Inertial Technology, *Springer*, 1998.